ANN-Enhanced Adaptive Sliding-Mode Control for STATCOM-Assisted Self-Excited Induction Generator in Wind Energy Conversion Systems

S. Radha Krishna Reddy[1*] Dr.J.B.V. Subrahmanyam[2], Dr. A. Srinivasula Reddy[3]

[1]*Research Scholar, EEE Dept, JNTU Hyderabad, Hyderabad, India
[2]Professor&Director, EEE Dept, Pallavi engineering College,JNTUH, Hyderabad, India
[3]Professor&Principal, EEE Dept, CMR Engineering College, JNTUH, Hyderabad, India

DOI: 10.64823/ijter.2604001

Date of Submission: Jan 27, 2026, **Date of Acceptance (Fast Track):** Feb 11, 2026, **Date of Publication:** April 7, 2026

***Abstract*:** The study introduces a new Adaptive Sliding-Mode Control approach that involves the application of artificial neural networks in the control of Static Synchronous Compensator systems coupled with Self-Excited Induction Generators of Wind Energy Conversion Systems. The proposed ASMC is guided towards enhancing the voltage regulation, reactive power support and stability at varying wind and fault conditions. The ASMC, in contrast to traditional Sliding-Mode Controllers (SMC) is an adaptive control system applying control gains dependent on system conditions reducing disturbances and improving resilience to parameter uncertainties and disturbances. The overall dq-axis plant model of SEIGSTATCOM system is constructed and simulated in MATLAB/Simulink to test the transient response, power quality and low-voltage ride-through (LVRT) capability. The results of simulation indicate that the ANN-enhanced ASMC has superior voltage stability and faster recovery in 40% voltage sags as a result of three-phase faults, and decreases Total Harmonic Distortion (THD) and reactive oscillations of power. The ANN-ASMC provides a smoother control action, better fault-ride-through, and smoother reactive power compensation in comparison with the SMC and PI controllers, which validates its use in the modern wind power systems that require high reliability and power quality.

***Index Terms*:** Adaptive Sliding-Mode Control, Static Synchronous Compensator, Self-Excited Induction Generator Wind Energy Conversion System

I. INTRODUCTION

The production of wind energy is becoming an important source of environmentally friendly energy with the need to improve the transmission capacity and effective operation of the system[1]. The integration of wind energy in the power systems poses three significant challenges that would make the wind energy conversion systems (WECS) to be developed and operated effectively. The system should be adequately reactive power controlled as it is critical in the process of keeping the voltage stable to the point of common coupling (PCC) during voltage dips and to meet low-voltage ride-through (LVRT) requirements[2]. They are done by using different techniques such as dynamic reactive power compensation and advanced control techniques to enhance LVVT capability[3];[4].

Self-excited induction generators (SEIG) are preferred among other types of generators because they are durable, cheap and have wide range of operation speed in standalone applications. Nevertheless, they require external power reactive support particularly in the case of the voltage drop, which is why VAR compensation[5] is crucial. Voltage-source inverter (VSI)-based flexible

alternating current transmission system (FACTS) apparatus[6][7][8], specifically the Static Synchronous Compensator (STATCOM) are typical solutions to improve the voltage regulation and stability of SEIG-based WECS [9][10].
In the control strategies, there has been a development in the aspect of managing the inherent challenges whereby the use of conventional proportional-integral (PI) controllers has been extensively used, and more sophisticated ones such as Linear Quadratic Regulator (LQR) [11][12], adaptive model reference control, and fuzzy logic-based controls[13]. Despite the different advantages of these methods, they usually require the manual parameter adjustment and may lack the capability to withstand uncertainties[14][15] [16]. Also, conventional PI and proportional-resonant (PR) controllers are not able to cope with bandwidth constraints, which undermines harmonic compensation. SMC methods have also become a strong competitor, with the ability to deal with uncertainty and system disturbance[17][18].

In single systems, PMSG and SEIG are used as primary sources[19], although strong designs are emphasised that provide low maintenance and costs[20]. New Lyapunov based control methods and RL based sliding mode control (RL-SMC) models are presented to improve the voltage stability and reactive power control, and the efficiency of these systems is supported by the supporting simulations of these systems under different conditions. The performance of the system is also improved by the introduction of AI in the sliding mode control, which have been illustrated with the help of simulation testing[21][22].
Moreover, the article [23] has the added value of improving voltage and frequency regulation of self-excited SCIG-based wind energy conversion systems by a grid-forming control structure. It controls reactive power and voltage with the help of a static compensator (STATCOM). Active power control approach measures the prime mover speed of the SCIG to maintain the active power of the STATCOM at zero balancing the active power of the system. The efficacy and accuracy of the framework can be demonstrated by simulation and testing results. Ali and Tariq [24] looked at the dynamic control techniques such as MPC, SMC, and AI, grid integration challenges, and variable-speed wind turbines. The results of simulation and performance comparison prove that these techniques can be effective in reducing power fluctuations and enhancing grid compatibility. The research finishes with large-scale wind energy integration control system possibilities and problems. In some small-scale standalone power generating systems, PMSG and SEIG are the main power producers. People use SEIG because of its dependable performance which allows operation in various environments and its affordable price and lightweight design and its ability to operate without maintenance needs and its ability to operate without maintenance needs from its brushless technology [25]; [26]. The researchers developed a Lyapunov control system which uses static synchronous compensator to maintain voltage stability during load changes for asynchronous generators. This would assist the generators in a better manner to control their voltage [27]. The system uses RL-based sliding mode control (RL-SMC) to control a hybrid-STATCOM which operates through model-free reinforcement learning (RL) to manage reactive power and harmonics. The RL-SMC has the characteristic of computer efficiency, constant accuracy, rapid responsiveness, and resilience. The agent-environment framework of RL and RL-SMC architecture are outlined. The performance of the RL-SMC is confirmed by simulations and experiments in different load and grid conditions [28]. In this work [29], the anti-disturbance capabilities offered by STSMC have been extended due to the application of AI. STSMC is originally aimed at the inner and outer loops of a wind energy transformation system based on DFIG. A compensation term based on ANN enhances convergence of STSMC and anti-disturbance. The ANN-based STSMC paradigm is confirmed by Matlab/Simulink processor in the loop (PIL) experiments.
The state-feedback control scheme of effective voltage regulation for SEIG–STATCOM systems but is not adaptive under very dynamic situations.
Finally, the suggestion of an Adaptive Sliding-Mode Control (ASMC) to the support of the SEIG systems in the context of the STATCOM implies that the voltage stability and dynamic responsiveness can be improved considerably and that the traditional drawbacks to the control approaches can be avoided. The extensive dq-axis model of SEIG-STATCOM systems indicates the bright perspectives of the application of the new approach to adaptive control in the modern wind energy systems, where the new controllers manage the situation significantly better than the traditional ones do. The new controller is synthesized through a comprehensive dq-axis model of the SEIG–STATCOM and tested under different load and wind conditions using MATLAB/Simulink simulations. The ASMC system outperforms traditional PI controllers and state-feedback controllers through its ability to maintain voltage stability and achieve lower total harmonic distortion (THD) and superior dynamic performance, which constitute essential requirements for contemporary wind power systems.

II. STATIC SYNCHRONOUS COMPENSATOR (STATCOM)

The static synchronous compensator This device functions as a reactive power compensation system which uses shunt connections to deliver voltage support by generating or absorbing reactive power at the shared connection point without needing any external reactors or capacitor systems.

Scheme of STATCOM Control

The control algorithm of the three-phase STATCOM operates through a D-Q synchronous control method which uses a single-phase D-Q control system. The D-Q frame theory of single-phase synchronous D-Q frame has been used to offer switching pulses to the three-phase STATCOM. The system operates through three phase voltages or currents which exist in the abc frame and undergo two transformations first to the 3-phase frame and then to the D-Q frame. The signal transformation process requires at least two phases to convert a signal into a fixed frame. The original signal refers to the component of the 90° lag signal of the stationary reference frame whereas the 90° lag signal refers to the component of the original signal. The PCC voltages (V_a V_b and V_c) monitor the currents (i_{sa} i_{sb} and i_{sc}) which pass through the sources and the load current (i_l) together with the bus voltage (V_{dc}). The system connects these three elements to create feedback signals which measure current and load and bus voltage. The system voltage or PCC voltage reaches its peak value when all PCC voltages function as balanced sinusoidal signals.

$$V_t = \sqrt{\frac{2}{3}(V_a^2 + V_b^2 + V_c^2)} \qquad (1)$$

The transformation of voltages and currents in a certain phase to a stationary a-b frame and, subsequently, the illustration of the PCC voltages and load currents in the stationary a-b frame are expressed as

$$V_{a\alpha}(t) = V_a(t),\ V_{b\alpha}(t) = V_b(t),\ V_{c\alpha}(t) = V_c(t) \qquad (2)$$

$$V_{a\beta}(t) = V_a(t - T/4),\ V_{b\beta}(t) = V_b(t - T/4),\ V_{c\beta}(t) = V_c(t - T/4) \qquad (3)$$

$$I_{l\alpha}(t) = I_l(t),\ I_{l\beta}(t) = I_l(t - T/4) \qquad (4)$$

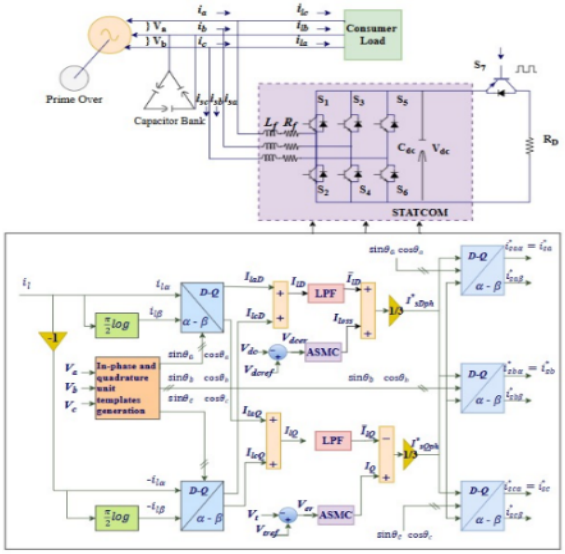

Figure 1 Block diagram of D-Q frame theory with STATCOM

But now assume a D- rotating at a rate synchronized

Frame is fit for phase a. This rotating along with $V_a(t)$. Q-axis and D-axis of phase a load current values are therefore approximated

$$\begin{bmatrix} I_{laD} & I_{laQ} \end{bmatrix} = \begin{bmatrix} cos\theta_a & sin\theta_a & -sin\theta_a & cos\theta_a \end{bmatrix} \begin{bmatrix} I_{l\alpha} & I_{l\beta} \end{bmatrix} \qquad (5)$$

Where, $cos\theta_a$ and $sin\theta_a$ are estimated using $V_{a\alpha}$ and $V_{a\beta}$ as follows:

$$\begin{bmatrix} cos\theta_a & sin\theta_a \end{bmatrix} = \frac{1}{\sqrt{(V_{a\alpha}^2 + V_{a\beta}^2)}} \begin{bmatrix} V_{a\alpha} & V_{a\beta} \end{bmatrix} \qquad (6)$$

The system uses a single-phase PLL structure based on a second order generalized integrator to estimate the value of θ. The PLL structure provides detection of both the utility's phase angle and its amplitude and frequency components. The diagram 2 indicates the overall outline of PLL.

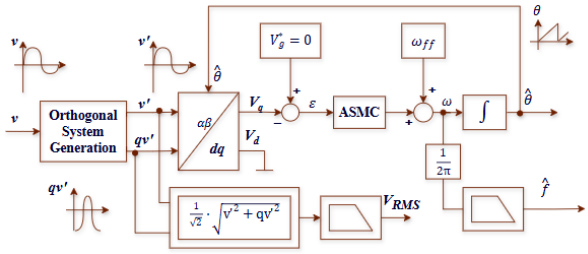

Figure 2 General Structure Of PLL

I_{laD} serves as the active power measurement for the load current because D-axis current estimation requires the multiplication and addition of signals that exist on the same axis. I_{laD} functions as the reactive power measurement for the load current because Qaxis current estimation requires the multiplication and addition of orthogonal signals. The load current D-axis and Q-axis values in phase "c" are estimated using the same method.

$$\left[I_{lcD}\ I_{lcQ}\right] = \left[cos\theta_c\ sin\theta_c\ -sin\theta_c\ cos\theta_c\right]\left[-i_{l\alpha}\ -i_{l\beta}\right] \qquad (7)$$

The negative current sign in equation (7) indicates that the load current for phase "c" matches the load current for phase "a" but operates 180 degrees out of phase. The single-phase load connects between phases "a" and "c" which results in no D-axis and Q-axis components being measured for phase "b". The D-axis values of the load current is provided as

$$I_{lD} = I_{laD} + I_{lcD} \qquad (8)$$

Equally, a similar Q-axis current component of load on the system is estimated as below

$$I_{lQ} = I_{laQ} + I_{lcQ} \qquad (9)$$

The total load-lug have corresponding photographs of D-axis and Q-axis electrons divided into two components, i.e. fundamental and oscillating components.

$$I_{lD} = \underline{I_{lD}} + \tilde{I}_{lD} \qquad (10)$$

$$I_{lQ} = \underline{I_{lQ}} + \tilde{I}_{lQ} \qquad (11)$$

The system's oscillatory component exists because its load serves nonlinearity and single-phase connected loads. The D and Q values obtained in (8) and (9) show an oscillating part because single-phase loads create unbalance although all connected loads operate in a linear manner. The D-axis and Q-axis components of the source currents must be free of these oscillatory components to measure power quality. The fundamental components are eliminated through low-pass filter operation.

The system needs to maintain the dc-bus capacitor voltage of the STATCOM at its target value through the measurement of capacitor voltage which is then compared to the target voltage and any existing voltage difference gets processed by a PI controller. The following formula shows the Vdc error for the STATCOM at sample point k.

$$V_{dcer}(k) = V_{dcref}(k) - V_{dc}(k) \qquad (12)$$

The STATCOM system measures its DC bus voltage at the kth sampling instant with its two voltage parameters $V_{dcref}(k)$ and $V_{dc}(k)$. The current study will set the dc-bus voltage reference value at 400 V. The PI controller output required to hold the voltage across the DC bus of the STATCOM constant to k th sampling point is given as

$$I_{loss}(k) = I_{loss}(k-1) + K_{pd}\{V_{dcer}(k) + V_{dcer}(k-1)\} + K_{id}V_{dcer}(k) \qquad (13)$$

I_{loss} represents the active component of current, which is also known as Daxis current component. This component needs to be supplied to the STATCOM because it serves to offset the system's operational losses. The dc-bus voltage PI-controller uses K_{pd} and K_{id} as its proportional and integrating gain constants. The source must provide the power loss term of the current (I_{loss}) and the filtered equivalent D-axis current term of the single-phase load estimated in (11). To provide balanced and sinuoidal source currents, all of the phases should have the same value of source currents in the D-axis after removal of compensation, and these currents should be free of any ripple. The D-axis component of the reference source current for each phase can be obtained by adding I_{lD} to Iloss and distributing the result equally among all phases.

$$I^*_{sDph} = \frac{\underline{I_{lD}} + I_{loss}}{3} \qquad (14)$$

I^*_{sDph} serves to represent the active power that the source should deliver after the system has received its compensation. The STATCOM needs to deliver reactive power because it must maintain the system voltage which includes PCC voltage together with the required power connection to SEIG and load. The ac voltage PI controller calculates the quantity of reactive power that the STATCOM will inject through its current output. The PCC voltage amplitude which was computed in equation (1) gets evaluated against the reference voltage. The PCC error at the kth sampling point Ver(k) gets defined through the following expression.

$$V_{er}(k) = V_{tref}(k) - V_t(k) \qquad (15)$$

The reference PCC voltage approximately reaches its peak value at V_{tref} while $V_t(k)$ represents the AC voltage strength measured at the PCC terminals during three phases of the observed waveforms at the kth time frame. The reference voltage is supposed to

maintain the PCC line voltage at 220 V. The PI controller output, in making the PCC voltage at the reference value at the kth sampling point, is expressed as

$$I_Q(k) = I_Q(k-1) + K_{pa}\{V_{er}(k) + V_{er}(k-1)\} + K_{ia}V_{er}(k) \quad (16)$$

Where, K_{pa} and K_{ia} are the proportional and integral gain constants of the PI controller, $V_{er}(k)$ and $V_{er}(k-1)$ are the error voltages at the kth and $(k-1)^{th}$ instant respectively. $I_Q(K)$ = the Q-axis or the reactive power component of the current that the STATCOM has to supply to meet the reactive power demand of both the load and the SEIG thus keeping the PCC voltage at the prescribed reference value. The current per phase of the reference source needed to regulate voltages within the system is referred to as the Q axis component of the reference current

$$I^*_{sQph} = \frac{I_Q - I_{lQ}}{3} \quad (17)$$

The variable I^*_{sQph} represents the amount of reactive power that needs to be supplied to each SEIG source phase in order to achieve the specified terminal voltage. The I^*_{sQph} value will show positive results when the system operates under certain loading conditions, but it will show negative results under all other conditions. The reference source current can be estimated through the D-axis and Q-axis current components derived from (15) and (18)according to the three specified measurement points of phase "a" and Ţ- axis and ù-axis components.

$$\left[i^*_{sa\alpha}\ i^*_{sa\beta}\right] = \left[cos\theta_a\ sin\theta_a\ -sin\theta_a\ cos\theta_a\right]\left[I^*_{sDph}\ I^*_{sQph}\right] \quad (18)$$

The α-axis current in the matrix above shows the reference source current for true phase "a" while the β-axis current shows the current that has a phase lag of $\pi/2$ which corresponds to the fake phase. As a result, it is possible to own

$$I^*_{sa} = I^*_{sDph}cos\theta_a - I^*_{sQph}sin\theta_a \quad (19)$$

Likewise, the approximate estimations of reference source currents of phase “b” and “c” are as follows

$$I^*_{sb} = I^*_{sDph}cos\theta_b - I^*_{sQph}sin\theta_b \quad (20)$$

$$I^*_{sc} = I^*_{sDph}cos\theta_c - I^*_{sQph}sin\theta_c \quad (21)$$

The currents of reference sources (I^*_{sa}, I^*_{sb}, and I^*_{sc}) are compared with the currents sensed on the source (i_{sa}, i_{sb}, and i_{sc}) and the current errors calculated as

$$i_{aerr} = i^*_{sa} - i_{sa} \quad (22)$$

$$i_{berr} = i^*_{sb} - i_{sb} \quad (23)$$

$$i_{cerr} = i^*_{sc} - i_{sc} \quad (24)$$

The current error indications are sent to the PWM pulse generator which uses current control to turn off the STATCOM IGBTs. The system generates PWM pulses which the STATCOM uses to obtain balanced sinusoidal source currents and their corresponding voltage control.

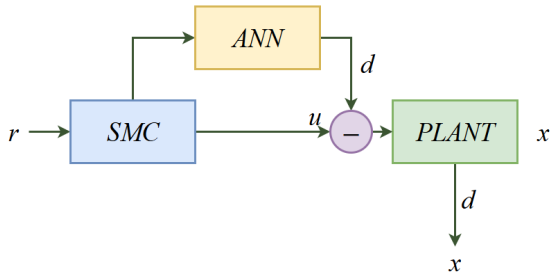

The system shown in the block diagram.

Fig represents an ANN-Enhanced Adaptive Sliding Mode Control (ANN–ASMC) framework, designed to improve robustness and adaptability in uncertain nonlinear systems. The overall structure integrates a Sliding Mode Controller (SMC) with an Artificial Neural Network (ANN) module to handle unmodeled dynamics and external disturbances affecting the plant. Nonetheless, here, the reference input r represents the desired system output. The SMC block generates the main control signal u u based on the sliding surface variable s, which is derived from the tracking error $e = r - x$. The ANN block receives system information (e.g., state or error data) from the SMC and estimates the lumped uncertainty d — which includes model inaccuracies, unknown nonlinearities, and external disturbances. It is estimated disturbance d d which is then adapted to compensate for the control signal before it is passed to the plant. The physical system or process under control is the plant which generates the actual output x. The subtractor (Σ) indicates that the control input u u is corrected by the ANN-estimated disturbance d, ensuring that the plant receives a disturbance-compensated signal. The output x of the plant is fed back to both the ANN estimator and SMC, forming a closed-loop system. The ANN-based controller that is constructed in this arrangement allows the system to learn and adapt its output in the real instances and at the same time ensure system reliability and provide accurate trajectory control with very little chattering. The system combines the strength of sliding mode control and the adaptive learning of ANN to generate an

efficient working system that yields an intelligent and robust control system that is adaptable to nonlinear, time-dependent as well as disturbance-prone environments.

III. SEIG TERMINAL VOLTAGE CONTROL

The d and q axes diagrams show the SEIG system together with its terminal capacitors and its STATCOM components. The mathematical models of the system present their dynamic behavior through differential equations which use stator currents and rotor flux linkage components as state variables according to (25)-(28). The stator and rotor flux linkages can be expressed in terms of stator and rotor currents by (29)–(32) [30].

$$v_{ds} = \left(R_s + \sigma L_s p\right) i_{ds} - \omega \sigma L_s i_{qs} + \frac{L_m}{L'_r} p\psi'_{dr} - \frac{\omega L_m}{L'_r} \psi'_{qr} \tag{25}$$

$$v_{qs} = \omega \sigma L_s i_{ds} + \left(R_s + \sigma L_s p\right) i_{qs} + \frac{\omega L_m}{L'_r} \psi'_{dr} + \frac{L_m}{L'_r} p\psi'_{qr} \tag{26}$$

$$v_{dr} = -\frac{L_m}{\tau'_r} i_{ds} + \left(\frac{1}{\tau'_r} + p\right) \psi'_{dr} - \left(\omega - \omega_r\right) \psi'_{qr} = 0 \tag{27}$$

$$v_{qr} = -\frac{L_m}{\tau'_r} i_{qs} + \left(\omega - \omega_r\right) \psi'_{dr} - \left(\frac{1}{\tau'_r} + p\right) \psi'_{qr} = 0 \tag{28}$$

Where, $\sigma = 1 - \left(L_m^2 / L_r' L_s\right)$

$$\psi_{ds} = L_s i_{ds} + L_m i'_{dr} \tag{29}$$

$$\psi_{qs} = L_s i_{qs} + L_m i'_{dr} \tag{30}$$

$$\psi'_{dr} = L'_r i'_{dr} + L_m i_{ds} \tag{31}$$

$$\psi'_{qr} = L'_r i'_{qr} + L_m i_{ds} \tag{32}$$

$$i_{dcs} = -\left(i_{ds} + i_{di} + i_{dl}\right) = Cpv_{ds} - \omega C v_{qs} \tag{33}$$

$$i_{qcs} = -\left(i_{qs} + i_{qi} + i_{ql}\right) = Cpv_{qs} - \omega C v_{ds} \tag{34}$$

It is possible to write the model of the SEIG and the capacitor in the stator voltage reference frame by substituting $pv_{qs} = v_{qs} = 0$ in equations (33 and 34).

$$pv_{ds} = -\frac{1}{C}\left(i_{qs} + i_{qi} + i_{ql}\right) \tag{35}$$

$$pv_{qs} = -\frac{1}{C}\left(i_{qs} + i_{qi} + i_{ql}\right) - \omega v_{ds} = 0 \tag{36}$$

$$p\psi'_{dr} = -\frac{L_m}{\tau'_r} i_{ds} - \frac{1}{\tau'_r} \psi'_{dr} + \left(\omega - \omega_r\right) \psi'_{qr} \tag{37}$$

$$p\psi'_{qr} = -\frac{L_m}{\tau'_r} i_{ds} - \left(\omega - \omega_r\right) \psi'_{dr} - \frac{1}{\tau'_r} \psi'_{qr} \tag{38}$$

$$pi_{ds} = \frac{1}{Z_2}\left[v_{ds} - Z_1 i_{ds} + \omega Z_2 i_{qs} + Z_3 \psi'_{dr} + \omega_r Z_4 \psi'_{qr}\right] \tag{39}$$

$$pi_{qs} = \frac{1}{Z_2}\left[-\omega Z_2 i_{qs} - Z_1 i_{ds} - \omega_r Z_4 \psi'_{qr} + Z_3 \psi'_{dr}\right] \tag{40}$$

Where

$Z_1 = R_s + \frac{L_m^2}{L_r' \tau_r'}; \quad Z_2 = \sigma L_s; \quad Z_3 = \frac{L_m}{L_r' \tau_r}; \quad Z_4 = \frac{L_m}{L_r'}$ Using a steady-state operating point that is computed from equations (35)–(40), the equations are linearised around this point.

$$\left(I_{ds} + I_{di} + I_{dl}\right) = 0 \tag{41}$$

$$\left(I_{qs} + I_{qi} + I_{ql}\right) = -\omega_o C v_{ds} \tag{42}$$

$$V_{ds} - Z_1 I_{ds} + \omega_o Z_2 I_{qs} + Z_{23} \wedge_{dr}' + \omega_r Z_4 \wedge_{qr}' = 0 \tag{43}$$

$$\omega_o Z_2 I_{qs} + Z_1 I_{ds} + \omega_r Z_4 \wedge_{qr}' - Z_{23} \wedge_{dr}' = 0 \tag{44}$$

$$\frac{L_m}{\tau_r'} I_{ds} - \frac{1}{\tau'} \wedge_{dr}' + \left(\omega_o - \omega_r\right) \wedge_{qr}' = 0 \tag{45}$$

$$\frac{L_m}{\tau_r'} I_{qs} - \left(\omega_o - \omega_r\right) \wedge_{dr}' + \frac{1}{\tau'} \wedge_{qr}' = 0 \tag{46}$$

$$P_1 = \frac{3}{2} V_{ds} I_{dl} \tag{47}$$

$$Q_1 = -\frac{3}{2} V_{ds} I_{ql} \tag{48}$$

The steady-state value of ωo is equal to 2*π* 50, while the value of V_{ds} is equal to 220* √2/3. The Ql value is calculated based on the load demand (P_l) and load power factor (p_f) that are provided. It is possible to derive idi as a function of iqi by beginning with the inverter loss model. The values of all variables are obtained by simultaneously solving this function as well as equations (41)–(48) in order to acquire the steady-state values. Using equation (36), the modest signal fluctuation in ω can be expressed as follows:

$$\Delta\omega = -\frac{\omega_o}{V_{ds}} \Delta v_{ds} - \frac{1}{C V_{ds}} \left(\Delta i_{qs} + \Delta i_{qi} + \Delta i_{ql}\right) \tag{49}$$

IV. Problem Setup

Consider an uncertain SISO plant:

$$\dot{x} = f(x,t) + g(x,t)u + d(t),$$
$$y = h(x) \tag{50}$$

Where $x \in R^n$, $u \in R$, $y \in R$, and $d(t)$ is an unknown matched disturbance. The control goal is to track a smooth reference $r(t)$ with tracking error $e := r - y$.

To simplify, consider a relative degree one error channel and describe the sliding variable

$$s := \dot{e} + \lambda e, \quad \lambda > 0. \tag{51}$$

V. Control Law with ANN Augmentation

The control input is described as follows:

$$u = u_{eq} + \hat{K} sat\left(\frac{s}{\phi}\right) + u_{AI} \tag{52}$$

where u_{eq} represents the nominal equivalent control, $\hat{K}$ denotes an adaptive bounded switching gain, and uANN addresses unmodeled dynamics by ANN estimation.

Boundary Layer: The function sat (ξ) represents the conventional symmetric saturation:

$$sat(\xi) = \{1, \xi > 1, \xi, |\xi| \le 1, -1\ \xi < -1, \tag{53}$$

and $\phi > 0$ determines the breadth of the boundary layer that reduces chattering.

ANN Compensation: The aggregated uncertainty is estimated using a trained model:

$$\hat{d}(x,t) = W^T \sigma(x), \qquad u_{AI} := -\hat{d}(x,t) \tag{54}$$

Where $\sigma(\cdot)$ is a feature map (e.g., RBF or polynomial), and W are the online-adapted weights.

Adaptive Laws

Bounded Switching Gain

A leakage-modified adaptation with projection ensures bounded gain:

$$\dot{\hat{K}} = \gamma|s| - \eta\hat{K}, \hat{K} \in [K_{min}, K_{max}], \quad (55)$$

Where, $\gamma, \eta > 0$

ANN Weight Update

The ANN weights are updated via gradient adaptation:

$$\dot{W} = -\Gamma\sigma(x)s, \Gamma = \Gamma^T > 0, \quad (56)$$

With projection to keep $W \in W$ (a compact set).

VI. Lyapunov Analysis

Define the estimation error $\tilde{d} := d - \hat{d}$ and $\widetilde{W} := W - W*$. the Lyapunov candidate is

$$V(s, \widetilde{W}) = \frac{1}{2}s^2 + \frac{1}{2}\widetilde{W}^T\Gamma^{-1}\widetilde{W} \quad (57)$$

Lemma 1: Sliding Dynamics. According to (50) -(56), the closed-loop dynamics

$$\dot{s} = -cs - \hat{K}sat\frac{s}{\phi} + \tilde{d} + \varepsilon \quad (58)$$

Where, $c > 0$ and ε denotes residuals.

Theorem 1 (Uniform Ultimate Boundedness). Given the projections on $\hat{K}$ and W, together with the constraints on $\tilde{d}$ and ε, the trajectories exhibit uniform ultimate boundedness (UUB). The bound radius diminishes with an increase $\hat{K}_{max}$, a drop in ϕ, and an enhancement in feature approximation.

$$\dot{V} \leq -cs^2 - \hat{K}|s|\ sat\left(\frac{|s|}{\phi}\right) + |s|(|\delta| + |\varepsilon|) + ||\widetilde{W}||\ ||\Gamma^{-1}\dot{W}*||. \quad (59)$$

Standard completion-of-squares arguments yield $\dot{V} \leq -\alpha\Psi(V) + \beta$, proving UUB.

Observation 1 (Chattering vs Robustness). The boundary layer ϕ trades accuracy for continuity; η mitigates gain drift while $\hat{K}_{max}$ constrains control effort.

VII. Discrete-Time Realization

For sampling time $T_s > 0$

$$e[k] = r[k] - y[k],$$

$$\dot{e}[k] \approx \frac{e[k]-e[k-1]}{T_s} \quad (60)$$

$$s[k] = \dot{e}[k] + \lambda e[k], \quad (61)$$

$$\hat{K}[k+1] = \prod_{[K_{min},K_{max}]} \left(\hat{K}[k]T_s(\gamma|s[k]| - \eta\hat{K}[k])\right), \quad (62)$$

$$W[k+1] = \prod_W (W[k] - T_s\Gamma\sigma(x[k])s[k]), \quad (63)$$

$$u[k] = u_{eq}[k] + \hat{K}[k]sat\left(\frac{s[k]}{\phi}\right) - W[k]^T\sigma(x[k]). \quad (64)$$

A first-order filter $u_f[k] = \alpha u[k] + (1-\alpha)u_f[k-1]$ can be used for actuators.

Design and Tuning

- Surface: Choose λ for desired transient behaviour.
- Boundary Layer: Set ϕ at 1–5% of typical $|s|$.
- Gain Law: Tune γ, η for desired reaching and leakage.
- ANN Estimator: Select $\sigma(x)$ spanning nonlinearities.
- Sampling: Choose T_s small enough for accurate $s[k]$ estimation.

Algorithm 1

Algorithm 1 Discrete-Time ANN-Enhanced ASMC
1: Input: $r[k], y[k], x[k]$; parameters $\lambda, \phi, \gamma, \eta, \Gamma$; bounds $[K_{min}, K_{max}]$, W
2: $e \leftarrow r - y$; $\dot{e} \leftarrow (e - e_{prev})/T_s$; $s \leftarrow \dot{e} + \lambda e$
3: $u_{eq} \leftarrow$ nominal design (feedback linearization/LQR)
4: $\hat{K} \leftarrow \prod_{[K_{min},K_{max}]} \left(\hat{K} + T_s(\gamma|s| - \eta\hat{K})\right)$
5: $W \leftarrow \prod_W (W - T_s\Gamma\sigma(x)s)$

6: $u \leftarrow u_{eq} + \widehat{K} sat\left(\frac{s}{\phi}\right) - W^T \sigma(x)$

7: Apply u; update $e_{prev} \leftarrow e$

VIII. Simulation Results and Discussion

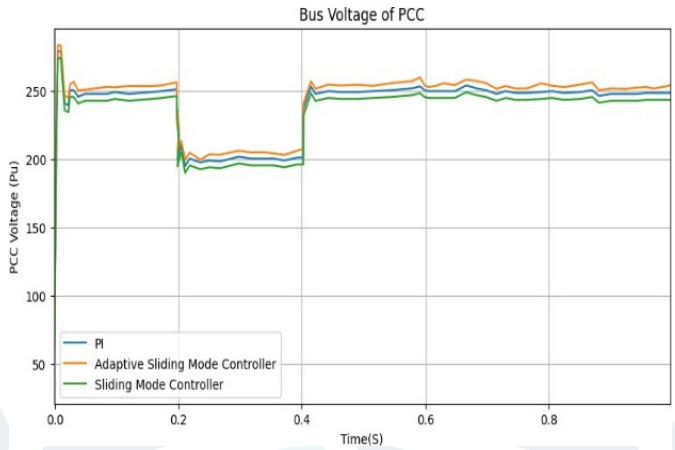

Figure 3: Performance under Static Load Condition

The section displays simulation findings which emerged from the MATLAB/Simulink system, which researchers established to assess how well the Adaptive Sliding-Mode Control (ASMC) system performs with the STATCOM-enabled SEIG system. The ASMC system undergoes complete testing against both the conventional Sliding-Mode Controller (SMC) and the standard Proportional-Integral (PI) controller. The research team developed two different testing situations to assess controller performance under two different conditions: the static load situation which tested transient performance and the fluctuating load situation which evaluated system robustness and adaptability. The assessment of each controller performance occurs through two evaluation methods which measure its dynamic response and power quality effects with Total Harmonic Distortion (THD) used as the main assessment factor.

Case 1: Performance under Static Load Condition

The system undergoes testing through static conditions to assess how each controller responds to dynamic situations. Figure 3 indicated that the dynamic response of the Point of Common Coupling (PCC) bus voltage indicates that three control strategies follow various system conditions, in particular, there is a large disturbance interval between 0.2s and 0.4s. The Adaptive Sliding Mode Controller continued to perform better throughout the simulation by having the highest voltage profile which is effective in reducing the magnitude of the voltage sag as opposed to the other counterparts. The PI controller was intermediate, even lower than the Adaptive controller, yet with a greater magnitude than the standard Sliding Mode Controller that also produced the lowest levels of voltage in both the steady-state and transient condition. This comparison brings to light the increased robustness of the Adaptive Sliding Mode Controller and its capacity to maintain the voltage stability in the case of critical disturbance events.

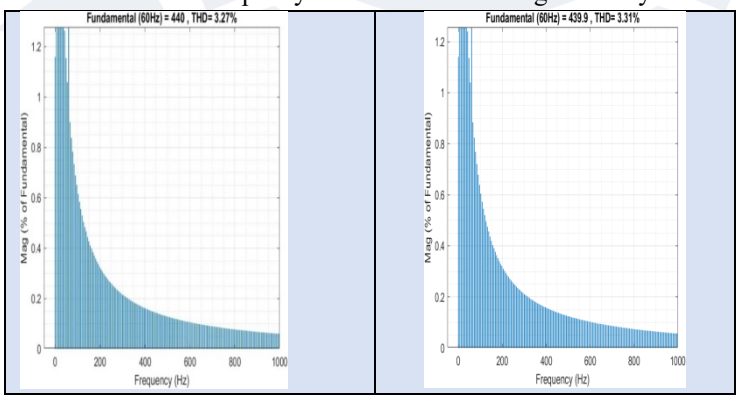

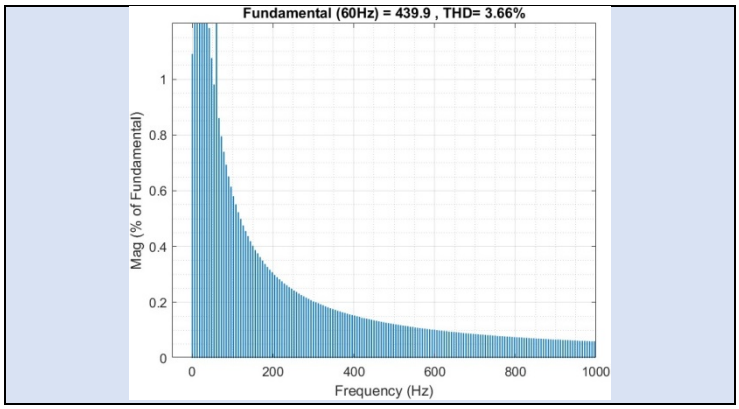

Figure 4: Total Harmonic Distortion (THD) of Load voltage of ASMC, SMC and PI controllers

Fig. 4 reveals the comparative Fast Fourier Transform (FFT) analysis of the system, maintained at a fundamental frequency of 60 Hz, demonstrated distinct variations in power quality across the three implemented control strategies. Although the Adaptive control was the best with a Total Harmonic Distortion (THD) of 8.68% (Fundamental: 427.2) and Proportional-Integral (PI) controller showed the slight improvement with the same of 8.62% (Fundamental: 427.3), the Sliding Mode control was the most effective methodology. The Sliding Mode strategy demonstrated the best way to reduce harmonic interference by the lowest THD of 8.40% and the largest fundamental of 427.6, which makes sense regarding its capacity to reduce the overall signal purity compared to the Adaptive and PI strategies.

CASE 2: WIND SPEED VARIATION

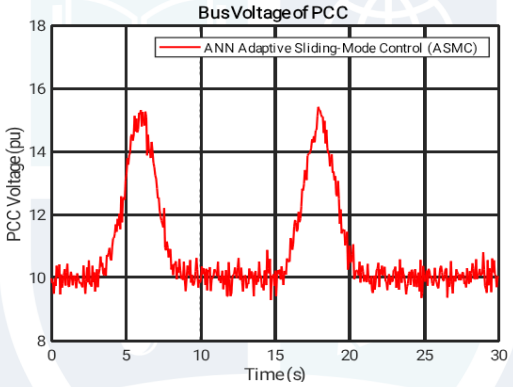

Figure 5: Combined wind speed variation

The study evaluates SMC and ASMC performance using combined wind speeds from constant wind, gradient wind, gust wind, and dry wind. The wind speed is maintained at 10 m/s. The gust of wind begins at 5 seconds and last for 5 seconds, reaching a maximum speed of 16 m/s. The gradient wind starts to rise at 1 meter per second from 15 seconds to 5 seconds, then suddenly drops to 10 meters per second. The PCC bus contains two 15 Mvar ASMC and SMC devices which researchers use for performance testing. The DFIG operates near unity power factor to simplify its control functions. Figure 9(a) displays how PCC voltage active performance reacts to wind speed changes. The point of common coupling voltage experiences fluctuations because the control systems do not inject reactive current into the system. ASMC outperforms SMC in grid voltage stabilization because it provides faster response times and higher reactive power delivery at the same capacity, as shown in Figure 9(b). The example study shows no transient instability, yet the system can scale up to operate larger wind power facilities.

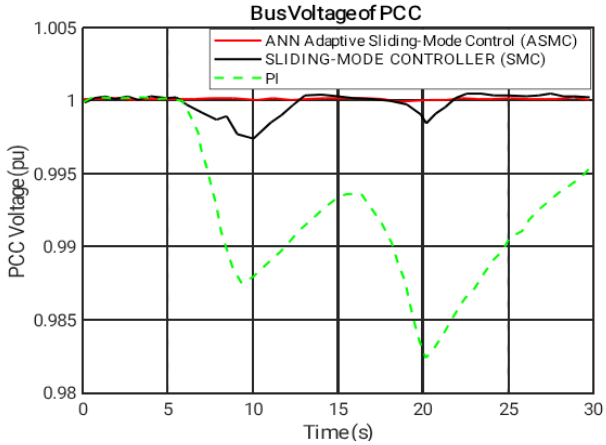

Figure 6: Bus voltage of PCC

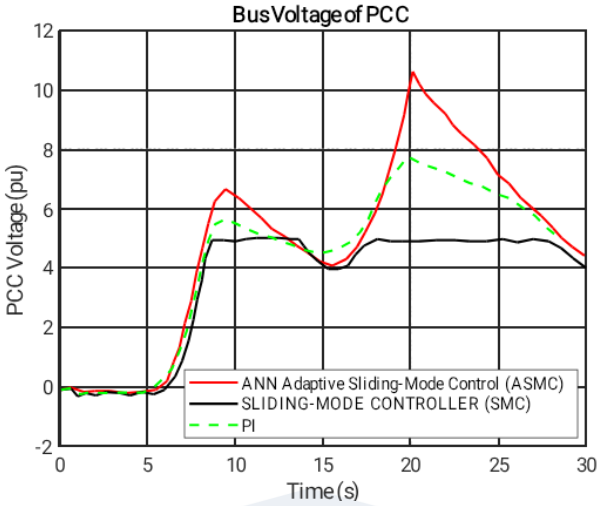

Figure 7: Compensations of Reactive power of Wind Speed Variation

CASE 3: GRID FAULT

The bus 1 location in Figure 8 experiences a transient three-phase fault which begins at 1 second and lasts for 0.15 seconds. The system uses a 0.5 seconds inactive period for the Crowbar protection because its rotor protection device activates due to rotor winding current. The three different reactive power management methods test system voltage control through three different methods which include SMC ASMC and no compensation method. At the PCC an ASMC and SMC of 10 Mvar each is mounted separately. Figure 9 shows that ASMC provides high-quality compensation, which is able to restore the normal system voltage. Upon fault clearance, ASMC supplies around 26 Mvar of reactive power, while SMC contributes just about 9 Mvar, insufficient to completely restore the system voltage. The performance disparity occurs since ASMC can provide up to 264% of its rated power for brief intervals, facilitating fast voltage restoration. The capacity of the utility is not enough for city-wide recovery at full voltage levels.

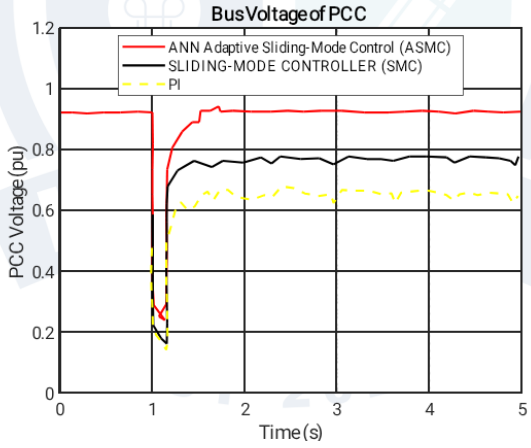

Figure 8: PCC bus voltage of Grid fault

A. SCENARIOS WITH 40% 1s VOLTAGE DIPS

At time 1 second a three-phase fault generated a symmetrical voltage sag which reduced voltage by approximately 40%. The Point of Common Coupling (PCC) voltage demonstrates its transient and steady-state behavior through two testing conditions SMC and ASMC which appear in Figure 9.

The ASMC scheme has a faster recovery and a better disturbance rejection ability than the controllers during the disturbance interval (1s 2s) a significant voltage dip is observed. PCC voltage with ASMC is more stable and less oscillatory and recovers the nominal value more quickly after the fault has been cleared. Contrary to this, the traditional SMC exhibits a larger voltage drop and slower dynamic response, which implies that it is less resilient to sudden symmetrical faults.

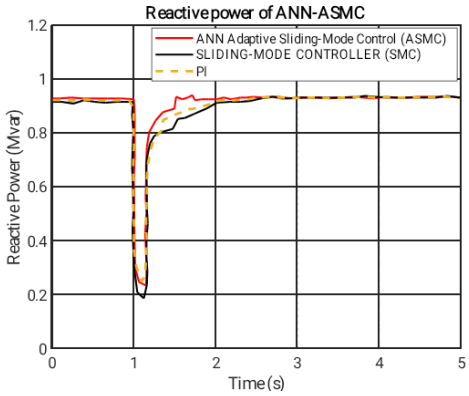

Figure 9: Point of Common Coupling (PCC) voltage under both SMC and ASMC

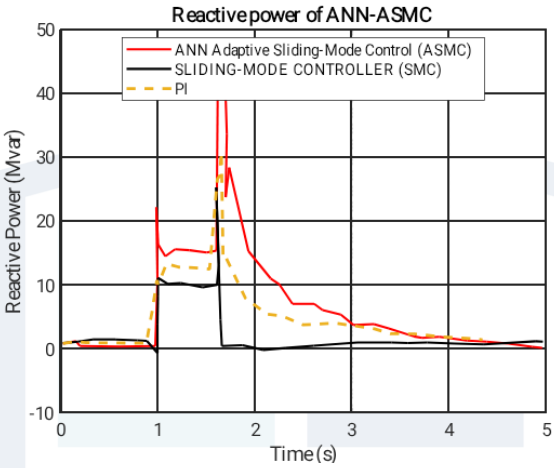

Figure 10: Reactive power of ANN-ASMC

These are figures (6 to 10) which are jointly used to analyse the performance of ANN Adaptive Sliding-Mode Control (ASMC), standard Sliding-Mode Control (SMC) and PI controller in stabilization of power systems. However, the ASMC (red line) is the quickest and most efficient voltage recovery when the voltage drops severely in a short-term (at t=1 second, the ASMC (red line) maintains the PCC voltage at a higher-level after the fault compared to the SMC and particularly the PI controller, which recovers gradually to the lowest voltage. This is a better transient performance of the ASMC that is obtained by a high-peak reactive power injection (greater than 40 MVAR) at the fault time. On a long-term transient, on the other hand, the ASMC is the most stable at a voltage of virtually 1.0 PU with little variability. This means that in this steady-state case, the ASMC is also more efficient and the reactive power compensation of the system is much smoother and of lower magnitude than in the normal SMC. To conclude, the results allow conclusively that the ASMC is the most robust control strategy that offers a great deal of dynamic response amid faults and a high degree of stability with effective control effort under normal operation.

IX. Conclusion

The analysis performed in this research paper has been able to demonstrate the enhanced operation of the designed ASMC scheme to a STATCOM-controlled SEIG system in a Wind Energy Conversion System (WECS) scenario. The adaptive control design is able to enhance stability of voltage, reactive power compensation and transient performance when faced with variable loads and wind conditions. The ASMC approach was contrasted to the traditional schemes of ProportionalIntegral (PI) and Sliding-Mode Control (SMC) by the simulations of the ASMC approach with MATLAB/Simulink. The findings confirmed that ASMC is able to reduce the chattering phenomenon that is present in conventional SMC in addition to offering faster dynamic recovery, reduced overshoot, and Total Harmonic Distortion (THD). Under conditions of wind speed variation, grid faults and symmetrical voltage sags (up to 40%), ANN-ASMC was very robust as the control gain is dynamically adjusted during system disturbances, with stable performance and the system is High Voltage Ride through (LVRT) capability. The controller ensured that there were good voltages in the transient conditions as the reactive power flow between the generator and the grid was controlled. This system was able to maintain the power quality and regulate the point of common coupling (PCC) voltage to be within acceptable limits. This proves the suitability of the controller in the modern renewable energy systems where flexibilities and dependability are the key factors. On the whole, ANN-Adaptive Sliding-Mode Controller can be viewed as a possible, low-complexity and high-performance solution to SEIG-STATCOM-based WECS application. Its flexibility to uncertainties, small computing power and

resistance to grid disturbance make it a formidable competitor of real-time operation in dispersed and stand-alone wind power systems.

X. REFERENCES

[1] Y. Tang, H. He, J. Wen, and J. Liu, "Power system stability control for a wind farm based on adaptive dynamic programming," *IEEE Trans. Smart Grid*, vol. 6, no. 1, pp. 166–177, 2015, doi: 10.1109/TSG.2014.2346740.

[2] J. C. Smith, M. R. Milligan, E. A. DeMeo, and B. Parsons, "Utility wind integration and operating impact state of the art," *IEEE Trans. Power Syst.*, vol. 22, no. 3, pp. 900–908, 2007, doi: 10.1109/TPWRS.2007.901598.

[3] N. Espinoza, M. Bongiorno, and O. Carlson, "Novel LVRT testing method for wind turbines using flexible VSC technology," *IEEE Trans. Sustain. Energy*, vol. 6, no. 3, 2015.

[4] J.-Y. Ruan, Z.-X. Lu, Y. Qiao, and Y. Min, "Analysis on applicability problems of the aggregation-based representation of wind farms considering DFIGs' LVRT behaviors," *IEEE Trans. Power Syst.*, vol. 31, no. 6, pp. 4953–4965, 2016, doi: 10.1109/TPWRS.2016.2539251.

[5] M. I. Mosaad, N. I. Elkalashy, and M. G. Ashmawy, "Integrating adaptive control of renewable distributed switched reluctance generation and feeder protection coordination," *Electr. Power Syst. Res.*, vol. 154, pp. 452–462, 2018, doi: 10.1016/j.epsr.2017.09.017.

[6] E.-M. M. S., "Fault ride-through capability enhancement for self-excited induction generator-based wind parks by installing fault current limiters," *IET Renew. Power Gener.*, vol. 5, no. 4, pp. 269–280, Jul. 2011, doi: 10.1049/iet-rpg.2010.0123.

[7] P. W. Carlin, A. S. Laxson, and E. B. Muljadi, "The history and state of the art of variable-speed wind turbine technology," *Wind Energy*, vol. 6, no. 2, pp. 129–159, Apr. 2003, doi: 10.1002/we.77.

[8] R. B., M. P., and T. T., "Operational experiences of STATCOMs for wind parks," *IET Renew. Power Gener.*, vol. 3, no. 3, pp. 349–357, Sep. 2009, doi: 10.1049/iet-rpg.2008.0075.

[9] Wessels, N. Hoffmann, M. Molinas, and F. W. Fuchs, "STATCOM control at wind farms with fixed-speed induction generators under asymmetrical grid faults," *IEEE Trans. Ind. Electron.*, vol. 60, no. 7, pp. 2864–2873, 2013, doi: 10.1109/TIE.2012.2233694.

[10] S. W. Mohod and M. V. Aware, "A STATCOM-control scheme for grid-connected wind energy system for power quality improvement," *IEEE Syst. J.*, vol. 4, no. 3, pp. 346–352, 2010, doi: 10.1109/JSYST.2010.2052943.

[11] Hazrati and A. Jalilian, "Grid side harmonic current mitigation in DFIG-based wind plants," in *Proc. 17th Conf. Electr. Power Distrib.*, 2012, pp. 1–7.

[12] Y. Zhang, M. Cheng, and Z. Chen, "Load mitigation of unbalanced wind turbines using PI-R individual pitch control," *IET Renew. Power Gener.*, vol. 9, no. 3, pp. 262–271, Apr. 2015, doi: 10.1049/iet-rpg.2014.0242.

[13] W.-L. Chen and Y.-Y. Hsu, "Controller design for an induction generator driven by a variable-speed wind turbine," *IEEE Trans. Energy Convers.*, vol. 21, no. 3, pp. 625–635, 2006, doi: 10.1109/TEC.2006.875478.

[14] W.-L. Chen, W.-G. Liang, and H.-S. Gau, "Design of a mode decoupling STATCOM for voltage control of wind-driven induction generator systems," *IEEE Trans. Power Deliv.*, vol. 25, no. 3, pp. 1758–1767, 2010, doi: 10.1109/TPWRD.2009.2035915.

[15] L. G. Scherer, R. V. Tambara, and R. F. de Camargo, "Voltage and frequency regulation of standalone self-excited induction generator for micro-hydro power generation using discrete-time adaptive control," *IET Renew. Power Gener.*, vol. 10, no. 4, pp. 531–540, Apr. 2016, doi: 10.1049/iet-rpg.2015.0321.

[16] S. A. Deraz and F. E. Abdel Kader, "A new control strategy for a stand-alone self-excited induction generator driven by a variable-speed wind turbine," *Renew. Energy*, vol. 51, pp. 263–273, 2013, doi: 10.1016/j.renene.2012.09.010.

[17] Q.-N. Trinh and H.-H. Lee, "An advanced current control strategy for three-phase shunt active power filters," *IEEE Trans. Ind. Electron.*, vol. 60, no. 12, pp. 5400–5410, 2013, doi: 10.1109/TIE.2012.2229677.

[18] Torchani, A. T. Azar, S. Ahmed, A. R. Mahlous, and I. K. Ibraheem, "Sliding mode control based on maximum power point tracking for dynamics of wind turbine system," *Front. Energy Res.*, vol. 12, p. 1434695, 2024.

[19] V. C. Sekhar, K. Kant, and B. Singh, "DSTATCOM supported induction generator for improving power quality," *IET Renew. Power Gener.*, vol. 10, no. 4, pp. 495–503, Apr. 2016, doi: 10.1049/iet-rpg.2015.0200.

[20] B. Tischer, J. R. Tibola, L. G. Scherer, and R. F. de Camargo, "Proportional-resonant control applied on voltage regulation of standalone SEIG for micro-hydro power generation," *IET Renew. Power Gener.*, vol. 11, no. 5, pp. 593–602, Apr. 2017, doi: 10.1049/iet-rpg.2016.0857.

[21] B. Singh, S. S. Murthy, and R. S. R. Chilipi, "STATCOM-based controller for a three-phase SEIG feeding single-phase loads," *IEEE Trans. Energy Convers.*, vol. 29, no. 2, pp. 320–331, 2014, doi: 10.1109/TEC.2014.2299574.

[22] M. Qasim and V. Khadkikar, "Application of artificial neural networks for shunt active power filter control," *IEEE Trans. Ind. Informatics*, vol. 10, no. 3, pp. 1765–1774, 2014, doi: 10.1109/TII.2014.2322580.

[23] Y. Kazemi and M. M. Rezaei, "A grid forming control strategy for STATCOM-assisted isolated SCIG-based wind energy conversion systems," *Energy Syst.*, 2023, doi: 10.1007/s12667-023-00642-8.

[24] U. Ali and A. Tariq, "Advanced control strategies for wind energy conversion systems," *J. Adv. Electr. Electron. Eng.*, vol. 1, no. 2, pp. 69–78, 2025.

[25] V. B. M. Krishna, V. Sandeep, S. S. Murthy, and K. Yadlapati, "Experimental investigation on performance comparison of self-excited induction generator and permanent magnet synchronous generator for small-scale renewable energy applications," *Renew. Energy*, vol. 195, pp. 431–441, 2022.

[26] V. B. M. Krishna, V. Sandeep, and K. Prasad, "Experimental study on self-excited induction generator for small-scale isolated rural electricity applications," *Results Eng.*, vol. 18, p. 101182, 2023.

[27] Z. Zhang, P. Gong, and Z. Lu, "A Lyapunov theory-based SEIG–STATCOM voltage regulation control strategy," *Energies*, vol. 17, no. 19, 2024, doi: 10.3390/en17194992.

[28] C. Gong, W.-K. Sou, and C.-S. Lam, "Reinforcement learning based sliding mode control for a hybrid-STATCOM," *IEEE Trans. Power Electron.*, vol. 38, no. 6, pp. 6795–6800, 2023, doi: 10.1109/TPEL.2023.3247835.

[29] Sami, S. Ullah, S. U. Amin, A. Al-Durra, N. Ullah, and J. Ro, "Convergence enhancement of super-twisting sliding mode control using artificial neural network for DFIG-based wind energy conversion systems," *IEEE Access*, vol. 10, pp. 97625–97641, 2022, doi: 10.1109/ACCESS.2022.3205632.

[30] P. C. Krause, O. Wasynczuk, S. D. Sudhoff, and S. Pekarek, *Analysis of Electric Machinery and Drive Systems*, 2nd ed. Wiley, 2002.